Space Weather

RESEARCH ARTICLE
10.1029/2021SW002750

Special Section:
NOAA's Space Weather Missions and Instruments

Key Points:

- This paper includes a comprehensive description of Solar and Galactic Proton Sensor observations
- An overview of the September 2017 solar particle event observations is presented
- Results from cross-calibrations with Geostationary Operational Environmental Satellite-13 and 15 Energetic Particle Sensors are also included

Correspondence to:
B. T. Kress,
brian.kress@colorado.edu

Citation:
Kress, B. T., Rodriguez, J. V., Boudouridis, A., Onsager, T. G., Dichter, B. K., Galica, G. E., & Tsui, S. (2021). Observations from NOAA's newest solar proton sensor. *Space Weather*, *19*, e2021SW002750. https://doi.org/10.1029/2021SW002750

Received 27 FEB 2021
Accepted 1 JUL 2021

Observations From NOAA's Newest Solar Proton Sensor

B. T. Kress[1,2], J. V. Rodriguez[1,2], A. Boudouridis[1,2], T. G. Onsager[3], B. K. Dichter[4], G. E. Galica[4], and S. Tsui[4]

[1]Cooperative Institute for Research in the Environmental Sciences at CU Boulder, Boulder, CO, USA, [2]NOAA National Centers for Environmental Information, Boulder, CO, USA, [3]NOAA Space Weather Prediction Center (SWPC), Boulder, CO, USA, [4]Assurance Technology Corporation, Carlisle, MA, USA

Abstract Space weather instrumentation on board the National Oceanic and Atmospheric Administration's (NOAA's) newest Geostationary Operational Environmental Satellite (GOES)-R series includes the Solar and Galactic Proton Sensor (SGPS), which has been collecting data since January 8, 2017. SGPS supports real-time alerts of solar energetic particle events at the NOAA Space Weather Prediction Center (SWPC) and provides data to the space science community, advancing basic space science research and understanding of space weather effects on satellite systems. The first GOES-R series spacecraft, GOES-16, was launched on November 19, 2016. A series of solar particle events in September 2017 enabled cross-calibration of GOES-16 SGPS with the Energetic Particle Sensors on GOES-13 and -15. This paper is intended as a resource for SGPS data users, including comparisons with legacy GOES energetic particle measurements, corrections applied to SGPS Level-2 data, important caveats, background level fluxes, and measurements of trapped magnetospheric protons.

Plain Language Summary Instrumentation on board the National Oceanic and Atmospheric Administration's (NOAA's) weather satellites includes the Solar and Galactic Proton Sensor (SGPS), which is used by NOAA Weather Prediction Center to monitor the radiation hazard to spacecraft systems and humans in space from energetic solar protons. A series of solar particle events in September 2017 enabled comparisons of SGPS measurements with the Energetic Particle Sensors on NOAA's older Geostationary Operational Environmental Satellite (GOES)-13 and -15 spacecraft. Comparisons with legacy GOES energetic particle measurements are critical for establishing consistent long-term data sets and understanding changes in long-term trends in solar energetic particle event fluxes.

1. Introduction

Since their inception, the National Oceanic and Atmospheric Administration's (NOAA's) geosynchronous weather satellites have carried instrumentation for space weather monitoring. The Space Environment Monitor (SEM) (Grubb, 1975) has been flown on board NOAA's geosynchronous weather satellites beginning with the Synchronous Meteorological Satellites SMS-1 and -2 (1974–1976) and followed by the Geostationary Operational Environmental Satellites (GOES)-1 up through GOES-15 (1975–present). SEM consists of three sensor systems, an Energetic Particle Sensor (EPS), a magnetometer, and a solar X-ray instrument. GOES space weather instruments provide space environment data in real time to NOAA's Space Weather Prediction Center (SWPC).

The original SEM EPS was primarily intended to monitor the radiation hazard to spacecraft systems and humans in space from 10 to 100s of MeV protons produced during solar proton events (SPEs). The first EPS measured protons in seven energy channels spanning 0.8–500 MeV, alpha particles in six channels spanning 4–392 MeV, and electrons with a single >2 MeV channel. The proton and alpha energy ranges were extended down to 0.8 and 4 MeV, respectively, to also observe the role of trapped magnetospheric protons and alphas in geomagnetic storms and substorms. The electron channel was included "primarily to provide an independent monitor of the electron environment critical to the X-ray sensor performance" (*Grub*, 1975), due to electron contamination in the X-ray sensor.

EPS has undergone a series of enhancements of its capabilities since. The EPS flown aboard GOES-13, -14, and -15 measures electrons from 30 keV to several MeV and protons from 80 keV to 100s of MeV (Hanser, 2011). Along with EPS, a High Energy Proton and Alpha Detector (HEPAD) was flown on GOES-4 through GOES-15.

HEPAD measures high energy proton fluxes above ~350 MeV in four broad channels (Raukunen et al., 2020, and references therein).

The Energetic Proton, Electron, and Alpha Detectors (EPEADs) flown on board GOES-13, -14, and -15 provide measurements similar to the original EPS, and "EPS" has become an umbrella name for both keV and MeV detectors on board GOES. The EPS/EPEAD component of the GOES energetic particle sensors (henceforth simply EPS) has remained unchanged since GOES-4, except for detector redesign for GOES-8 (Rodriguez et al., 2014). The final SEM EPS, flown on board GOES-15, stopped collecting data in March 2020 when GOES-15 was placed in storage mode.

Rodriguez et al. (2014) presented results from intercalibration of GOES 8–15 solar proton detectors, demonstrating the consistency of EPS measurements since 1994. The period of overlap between GOES I-M and NOP series (GOES 8–12 and 13–15) included the December 2006 SPEs, providing SEP data for the intercalibration of EPS instruments on board those two GOES series. Cross-calibration of SEP channel measurements from detectors at different local times is possible when the channel bandpass energies are above local proton cutoff energies at respective spacecraft locations and in directions of arrival within the detector fields of view (Kress et al., 2013; Rodriguez et al., 2014). Under quiet geomagnetic conditions, SEP fluxes at geosynchronous up to several 10s of MeV are not in general isotropic or the same at different local times. Under disturbed magnetospheric conditions, geomagnetic shielding is suppressed and SEP fluxes may become isotropic and homogeneous along geosynchronous orbit. Rodriguez et al. (2014) show that during periods of high solar wind dynamic pressure, the cutoff is suppressed sufficiently for cross-calibration of EPS channels ≥4.2–8.7 MeV. The December 14, 2006 SPE included an ~10h period with P_{dyn} >10 nPa that enabled cross-calibrations between GOES-13 and -10.

With the launch of NOAA's new GOES-R series, EPS and HEPAD have been replaced with an entirely new suite of energetic particle detectors. The first of NOAA's GOES-R series spacecraft, GOES-16, was launched on November 4, 2016. GOES-16 replaced GOES-13 as NOAA's GOES East operational satellite at 75.2°W on December 18, 2017. GOES-R series instrumentation includes the new Space Environment In-Situ Suite (SEISS) (Dichter et al., 2015; Kress et al., 2020), designed, assembled and calibrated by the Assurance Technology Corporation (ATC). SEISS is composed of five particle sensor units: A low-energy magnetospheric particle sensor (MPS-LO) for monitoring spacecraft charging, a high-energy magnetospheric particle sensor (MPS-HI) for measuring radiation belt electrons and ring current protons, two Solar and Galactic Proton Sensor (SGPS) units (east and west facing), and an Energetic Heavy Ion Sensor (EHIS). Measurement of 30 eV–30 keV electrons and ions by MPS-LO and 30 species of heavy ions (He-Ni) by EHIS are new capabilities not previously flown on the GOES system.

SGPS measures protons with energies from 1 to >500 MeV in 14 energy channels, filling the role of the original EPS measurements. The primary operational use of SGPS is to support SWPC's real-time alerts of solar energetic proton events, which can cause single-event effects (SEEs) in space electronics (Tylka et al., 2005) and excessive radiation dose in humans in space and at commercial aviation altitudes over the poles (Dyer et al., 2003). During a solar particle event, >10 MeV protons penetrate below 100 km altitude, producing ionization that disrupts HF communication and navigation in the polar regions (Clilverd et al., 2005). GOES SEP measurements also provide real-time input for atmospheric radiation and polar cap absorption (PCA) models (Mertens et al., 2010; Rose & Ziauddin, 1962; Sauer & Wilkinson, 2008). The GOES-16 SGPS has been returning data in real time since January 8, 2017. A second SGPS was launched on GOES-17 on March 1, 2018. GOES-17 replaced GOES-15 as NOAA's GOES West operational satellite on February 12, 2019 at 137.2°W. GOES-T and -U are currently scheduled for launch in 2021 and 2024, respectively.

The July and September 2017 SPEs enabled cross-calibration between SGPS and EPS. Since the July and early September 2017 SPEs did not produce significant response in SGPS channels >25 MeV, the cross-calibration results included in this paper are mainly focused on the September 10–11, 2017 GLE (ground level enhancement of SEP secondaries, observed by neutron monitors). Unfortunately, September 10–11, 2017 was a geomagnetically quiet period restricting the cross-calibrations to energy channels $\gtrsim$ 40 MeV. During the July 2017 SPE, there was a brief period of high solar wind dynamic pressure with the potential for cross-satellite calibrations of channels with energies normally below geomagnetic cutoffs; however, a soft spectrum and low count rates limit the usefulness of this event. This paper includes results from comparisons between SGPS and EPS energy

Table 1
GOES-R Series SGPS Proton Energy Channels by Telescope

SGPS Tel. 1	SGPS Tel. 2	SGPS Tel. 3	EPS/EPEAD
P1: 1.0–1.9	P6: 25–40	P8A: 83–99	P1: 0.74–4.2
P2A: 1.9–2.3	P7: 40–80	P8B: 99–118	P2: 4.2–8.7
P2B: 2.3–3.4		P8C: 118–150	P3: 8.7–14.5
P3: 3.4–6.5		P9: 150–275	P4: 15–40
P4: 6.5–12		P10: 275–500	P5: 38–82
P5: 12–25		P11: >500	P6: 84–200
			P7: 110–900

Note. EPS/EPEAD energy channels (from the GOES-N Series Data Book) are also shown in the right column for reference. All energies are expressed in MeV. EPEAD, Energetic Proton, Electron, and Alpha Detectors; EPS, Energetic Particle Sensor; GOES, Geostationary Operational Environmental Satellites; SGPS, Solar and Galactic Proton Sensor.

channels. The cross-satellite comparisons reveal systematic differences between SGPS and EPS. Quantification of the differences between the SGPS and EPS measurements is critical for understanding changes in long-term trends in SPE fluxes and accounting for changes in space weather model results where legacy GOES energetic particle measurements have been used as model inputs.

This paper provides a comprehensive description of SGPS measurements for SGPS data users, beginning with a description of SGPS in Section 2 and a brief overview of its ground calibrations in Section 3. For more detailed descriptions of SGPS design, operation, and ground calibrations, see (Dichter et al., 2015). Level-1 and Level-2 data are described in Section 4. Techniques for recovering a spectrum from reported fluxes are included in Section 5. Examples of SGPS observations are presented in Sections 6 and 7, including first-light observations of magnetospheric protons and data from the September 2017 SPEs, now available from NOAA's National Centers for Environmental Information (NCEI) website (https://www.ngdc.noaa.gov/stp/satellite/goes-r.html) under the special events data tab. Results from cross-calibrations with GOES EPS, mainly from the September 2017 events, are presented in Section 8. This is followed by descriptions of corrections applied to Level-1 and Level-2 data and remaining measurement anomalies in Section 9, and finally, summary and discussion in Section 10.

2. Instrument Description

There are two SGPS units mounted on each GOES-R series spacecraft facing in the spacecraft −X and +X directions. When the spacecraft is not in the yaw-flipped configuration, SGPS−X faces west and SGPS+X faces east. Each SGPS unit has three solid-state (silicon detector) telescopes T1, T2, and T3 for measuring 1–25, 25–80, and 80–500 MeV protons, respectively. All three telescopes have the same look direction (i.e., +X or −X). T1 and T2 have 60° full cone angle fields of view, and T3 has a 90° full cone angle field of view (FOV). Each unit measures 1–500 MeV proton fluxes in 13 logarithmically spaced differential channels (P1–P10) and >500 MeV proton flux in a single integral channel (P11). The SGPS energy channels are shown in Table 1. The energy bands given in Table 1 are nominal/design energies. SGPS channel energy bounds determined from ground calibrations are included in Appendix B.

SGPS also provides 1-s cadence alpha particle counts in 12 channels in Level-0 data. However, at the time of writing, the alpha particle data are not processed in the real-time GOES-R data stream. Work to include alpha particle fluxes in the SGPS Level-1b (L1b) and Level-2 data is under way. The SGPS alpha particle measurements are not covered in this paper.

3. Ground Calibration Overview

All SGPS units were ground calibrated at beam facilities including the following: University of California at Davis Cyclotron Laboratory, Francis S. Burr Proton Therapy Center at Massachusetts General Hospital, NASA Space Radiation Laboratory at Brookhaven National Laboratory, and Massachusetts Institute of Technology Electron Accelerator (to investigate electron contamination). Tests of SGPS P11 (> 500 MeV proton channel) were also performed at ATC Chelmsford using cosmic ray muons. In general, each SGPS channel was calibrated with 4–8 beam energies spanning the in-band portion of the channel, with special care to capture the channel turn-on energy. Angular responses within the FOV were determined in 5° increments with respect to the collimator center line, assuming azimuthal symmetry. Additional tests were performed to characterize the side and rear entry and out-of-band responses.

In addition to ground calibrations, SGPS channel responses were simulated using the GEANT4 (GEometry ANd Tracking) code (henceforth simply GEANT), which models the passage of particles through matter using Monte

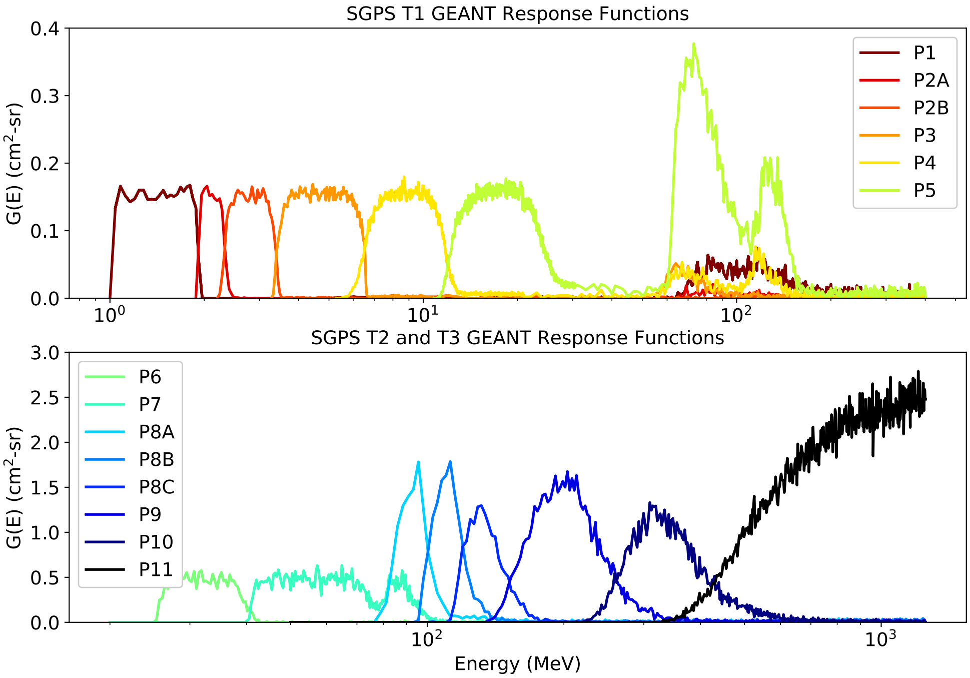

Figure 1. Solar and Galactic Proton Sensor channel responses, simulated using GEANT4 (GEometry ANd Tracking) code. The GEANT4 response functions are vertically scaled and/or shifted in energy for best-fit agreement with beam calibrations and then used to compute channel geometric factors.

Carlo methods (Agostinelli et al., 2003). The SGPS GEANT response functions for channels P1–P11 are shown in Figure 1. Some noteworthy features of the GEANT functions, which are borne out by ground calibrations and on-orbit observations, are the T1 out-of-band high energy islands near 100 MeV and the P7 secondary island due to rear entry particles at 80–100 MeV. An instrument level correction is used to remove the P7 80–100 MeV secondary island. The GEANT response functions are vertically scaled and/or shifted in energy for best-fit agreement with ground/beam calibrations to obtain the response functions used to compute channel geometric factors.

An energy-dependent geometric factor $G(E)$ (cm^2-sr) for a given channel is obtained by integrating effective area $A(E,\theta)$ over the FOV of the detector

$$G(E) = \int_{FOV} A(E,\theta)\, d\Omega, \tag{1}$$

where the integration is performed over the nominal instrument FOV given above in Section 2. The effective area is dependent on energy, E, and the angle of incidence with respect to the center line of the detector collimator, θ, and is independent of the azimuthal angle about the collimator look direction.

Each energy-angle measurement yields a corresponding effective area $A_{i,j}$, where i is the angle index and j is the energy index. The integral above is approximated using the empirically determined effective areas

$$G_j = 2\pi \sum_{i=1}^{\text{num. angles}} A_{i,j} \sin\theta\, d\theta, \tag{2}$$

yielding discrete energy-dependent geometric factors G_j. Response functions $G(E)$ for each channel are obtained by scaling the GEANT modeled response functions to minimize RMS difference with the empirically determined G_js in the in-band portion of the channel. In some cases, when there is a significant difference between the GEANT functions and G_js, the GEANT functions are also shifted in energy. The standard deviation of the empirically determined G_js with respect to the modeled response functions, after shifting and/or scaling, is taken as an estimate of the instrument error, σ_G, associated with the channel geometric factor G_0 defined below in Section 4.

The FWHM points of the response functions are taken as the lower (E_L) and upper (E_U) channel energy bounds, and the energy integrated channel geometric factors are obtained

$$G = \int_{E_1}^{E_2} G(E)\, dE, \tag{3}$$

where the integration limits E_1 and E_2 are chosen to bound the in-band portion of the response function.

3.1. Cautionary Note

SGPS differential channels were calibrated with beam energies in a narrow band, at 4–8 energies spanning the in-band portion of each channel. The geometric factors obtained from ground calibration provide a measurement of the differential flux at the effective energy of the "in-band" portion of the response function, with the assumption that the counts from the high energy tail or high energy islands contribute a relatively small fraction of the total counts. This condition is met under conditions with a steep energy spectrum (e.g., $\gamma \sim 2$ in Equation 8 below). This assumption is typically violated in two cases, (1) at the onset of a SPE when there may be a very hard spectrum and (2) during quiet periods when counts are mainly from galactic cosmic rays (GCRs). SGPS does not necessarily provide an accurate flux measurement in these cases.

4. Ground Processing

Complete descriptions of GOES-R data variables, units, dimensions, etc. are given in the Product Definition and User's Guide (PUG, available at https://www.goes-r.gov/resources/docs.html). The L1b PUG gives an overview of the L1b ground processing system and complete descriptions of L1b data. Level-2 (L2) data from the space weather instruments onboard GOES-R is described in the L2 Algorithm Theoretical Basis Documents (ATBDs) to be made available from NCEI's GOES-R website. The L2 ATBDs describe the theoretical basis of the algorithms, assumptions and limitations, exception handling, inputs and outputs, and data flow.

4.1. Level-1b Processing

Each SGPS unit provides proton counts accumulated over a 1-s interval from 13 differential channels and one integral channel. Counts in Level-0 data are converted to 1-s cadence fluxes in L1b processing. SGPS L1b processing includes unpacking L0 data, dead-time corrections, out-of-band contamination and/or background removal, and conversion from count rates to differential directional number fluxes $(\mathrm{cm}^2\text{-s-sr-keV})^{-1}$. Currently, P5, P8C, P9, and P10 have out-of-band removal steps implemented in L1b processing; however, out-of-band removal coefficients are set to zero, and these are not in use. At the time of writing, work is ongoing to determine sources of backgrounds and correct values for out-of-band removal coefficients.

The reported GOES differential flux in a given energy channel is calculated operationally

$$j_{\mathrm{reported}} = \frac{C}{G}, \tag{4}$$

where C is the count rate and G is the channel integrated geometric factor obtained from ground calibrations described above. In L1b processing, we adopt a rectangular model of the channel response function,

$$G = \begin{cases} 0 & \text{if } E \left\langle E_L \;\; or \;\; E \right\rangle E_U \\ G_0 & \text{if } E_L < E < E_U, \end{cases} \tag{5}$$

and G in Equation 4 is replaced with $G_0 \Delta E$ (i.e., set $G_0 = G/\Delta E$), where the channel width is $\Delta E = E_U - E_L$. L1b processing uses values for G_0, E_L and E_U from ground calibrations to convert counts to fluxes. The G_0, E_L and E_U values used in GOES-16 and -17 SGPS ground processing are provided in Appendix B.

L1b data also includes an estimate of the absolute error associated with the reported flux, which is obtained by adding the relative Poisson and instrument (geometric factor) error in quadrature and multiplying by the flux. The standard deviation of a Poisson distribution is the square root of its average value. In L1b processing, the square root of the counts from a single sample ($\sqrt{N}$) is used as an estimate of the Poisson error. In cases with low counts, this may be a poor estimate.

$$\sigma = j\sqrt{1/N + \sigma_G/G}. \tag{6}$$

The geometric factor errors, σ_G, used in GOES-16 and -17 ground processing are provided in Appendix B. Additional variables in the L1b NetCDF data files are described in the metadata (e.g., timestamps, data quality flags, etc.).

4.2. Level-2 Processing

SGPS Level-2 (L2) processing includes creation of 1 and 5 min averages, the differential-to-integral flux algorithm, solar particle event rate-of-rise, and solar particle event detection. The integral flux algorithm calculates proton integral fluxes from the 5-min averaged differential proton fluxes using the iterative approach described in Section 5 below. The solar particle event rate-of-rise and event detection algorithms are designed for SWPC's real-time SPE detection and forecast but also include event peak flux and event fluence outputs for retrospective use. Corrections for GOES-16 SGPS−X T1 and T3 temperature dependence and SGPS+X P7 anomalously low count rates are also applied in L2 processing (described in Section 9 and Appendix A).

We expect the SGPS L2 1 and 5-min averages of SPE fluxes to be of most interest to the retrospective user. A boxcar averaging of all valid data points within sequential 1 or 5-min intervals is performed. The error term provided with the L2 1 and 5-min averages is obtained similarly to the L1b errors, that is, using the total counts associated with the average, $N_{tot.}$, to estimate the Poisson error and adding the relative Poisson and instrument error in quadrature

$$\sigma_{avg.} = j_{avg.}\sqrt{1/N_{tot.} + \sigma_G/G}. \tag{7}$$

Additional variables in the L2 NetCDF data files are described in the metadata (e.g., timestamps, data quality flags, etc.).

5. Recovering an Ambient Spectrum From SGPS Measurements

A power law is usually used to model a SEP spectrum,

$$j(E) = j_0 E^{-\gamma}. \tag{8}$$

An effective center energy, $E_{\text{eff.}}$, must be associated with each flux measurement to fit (8) to measurements from a set of finite bandwidth energy channels. Ideally, this is the energy where the reported flux is equivalent to the ambient flux. In practice, the correct choice of effective energy depends on the desired accuracy and characteristics of the channel response functions. A simple approach that may provide an adequate approximation is to use the midpoint of the upper and lower channel energy bounds. This choice yields the correct flux when $\gamma = 0$, that is, the differential flux is constant and correct at all energies in the channel bandwidth.

A method that provides a better approximation for typically steep SEP spectra is to use the geometric mean of the channel energy bounds, $E_{\text{eff.}} = \sqrt{E_L E_U}$ (Kronberg & Daly, 2013; Lario et al., 1998). Assuming a rectangular channel response function, this formula is exact when $\gamma = 2$.

If additional accuracy is needed, or for very broad energy channels, a spectrum-dependent expression for $E_{\text{eff.}}$ may be derived as follows: The total count rate from a channel is the convolution of the response function $G(E)$ with the energy spectrum $j(E)$

$$C = \int_0^\infty j(E)G(E)dE, \tag{9}$$

Assuming that the energy spectrum is a power law and that $G(E)$ is sufficiently well behaved,

$$j_{\text{reported}} = j_0 E_{\text{eff.}}^{-\gamma} \Rightarrow E_{\text{eff.}} = \left[\frac{\int_0^{\infty} E^{-\gamma} G(E) dE}{G} \right]^{-1/\gamma} \tag{10}$$

If we use a rectangular function model of the response function, we obtain the analytic expression

$$E_{\text{eff.}} = \left[\frac{E_U^{1-\gamma} - E_L^{1-\gamma}}{\Delta E(1-\gamma)} \right]^{-1/\gamma} \tag{11}$$

Use of Equation 11 requires that γ is known a priori. This suggests the following iterative approach where observed fluxes are fit to a piecewise continuous sequence of power law functions $j = j_{0i} E^{-\gamma_i}$ (Rodriguez et al., 2017):

1. Initialize effective energies to geometric mean $E_{\text{eff.}} = \sqrt{E_L E_U}$.
2. Compute the spectral index between each pair of channels $\gamma_i = \dfrac{\log_{10}(j_{i+1}/j_i)}{\log_{10}(E_i/E_{i+1})}$.
3. Compute effective energies corresponding to each channel using Equation 11 with an average of bounding γs.
4. Iterate steps 2 and 3 to converge on effective energies.

If a single power law fit is desired (e.g., if the flux data are known to be noisy), a method similar to steps 1–4 above can be used to iteratively fit a single power law to a set of energy channels by replacing step 2 with a least squares fit to a single power law function and using the value obtained for γ in step 3.

If a rectangular function is a poor approximation of the channel response functions (e.g., due to a significant high energy tail and hard spectrum) and if the full response functions are known or can be estimated, then Equation (11) in step 3 above can be replaced with a numerical solution of Equation 10.

6. SGPS Measurements During Quiet Solar Conditions

The SGPS differential channels were designed and calibrated to measure SPEs. GCR fluxes in the P1–P9 (1–275 MeV) energy range are well below background levels in these channels. When interplanetary protons are not elevated above the GCR flux level, only channels P1, P2A, P2B, P10, and P11 provide valid proton flux measurements. When a SPE is not in progress, SGPS channels P1–P2B (1.0–3.4 MeV) usually measure trapped magnetospheric protons. Channels P10 (275–500 MeV) and P11 (>500 MeV) measure GCR fluxes.

6.1. SGPS Backgrounds

When interplanetary proton fluxes are not elevated, the reported fluxes in P3–P9 are at background levels. The primary source of backgrounds in P3–P9 is out-of-band GCR counts from the high energy tail portion of the channel response functions. Since the geometric factor is obtained from the area under the in-band portion of the response function only, when flux levels are sufficiently low the GCR counts from the high energy tail portion of the response function are a significant contribution to the total counts, and reported fluxes are significantly higher than actual GCR fluxes.

In early 2018, background levels in GOES-16 and -17 SGPS P3–P5 were ~10^{-5} (cm^2-s-sr-keV)$^{-1}$. Background levels in P6–P9 were ~$10^{-6} - 10^{-7}$ (cm^2-s-sr-keV)$^{-1}$. The backgrounds are significantly higher in P3–P5 partly due to the rising GCR spectrum up to ~400 MeV and also due to the high energy islands in the P1–P5 (T1) response functions seen in Figure 1. The P3–P9 backgrounds are several orders of magnitude above GCR flux levels, which in early 2018 extended from ~10^{-10} (cm^2-s-sr-keV)$^{-1}$ at 1 MeV to ~10^{-7} (cm^2-s-sr-keV)$^{-1}$ at the GCR spectrum peak near 400 MeV (from Matthiä et al. [2013] and Badhwar-O'Neill, 2014 [O'Neill et al., 2015] GCR models). Since the P10 energy band bounds the GCR spectrum peak, during quiet solar conditions it provides a calibrated measure of GCR flux. SGPS P10 GCR fluxes are generally within a factor of 2 of fluxes from the Matthiä et al. (2013) and Badhwar-O'Neill 2014 GCR models.

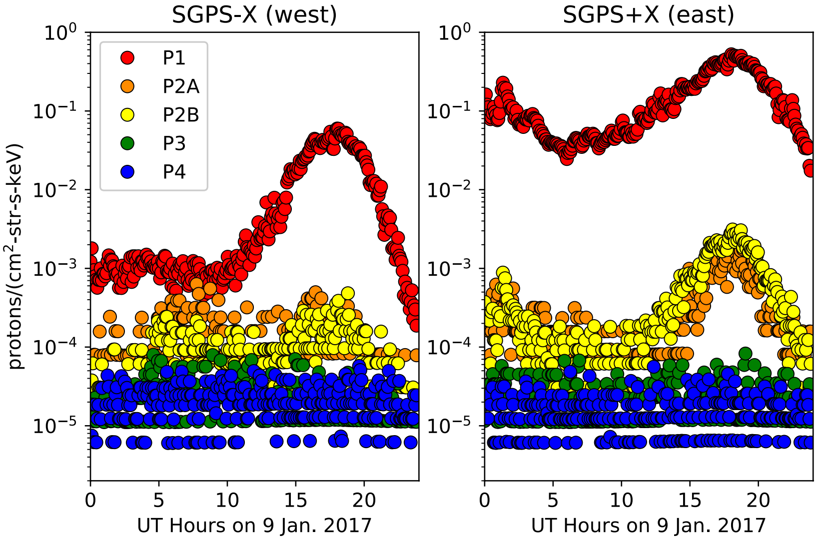

Figure 2. Geostationary Operational Environmental Satellites (GOES)-16 Solar and Galactic Proton Sensor (SGPS) P1–P4 5-min averaged proton fluxes from the first full day of data collection when GOES-16 was at 89° W longitude. Fluxes above background levels are seen only in P1, P2A, and P2B. The diurnal variations in flux and difference in flux levels between east- and west-facing units are expected (see accompanying text).

6.2. First Light: Magnetospheric Protons

Figure 2 shows 5-min averaged SGPS fluxes from P1 to P4 during the first full day of SGPS data collection on January 9, 2017. P2A and P2B are near background levels in the west-facing unit, and P3 and P4 are at background levels in both units. The diurnal flux variations and difference in flux levels between the east- and west-facing units are typical. GOES-16 was initially launched into the GOES storage/checkout location at 89° W longitude, thus was at noon local time (LT) near 18 UT. The maximum flux is near noon LT because proton drift shells extend to higher altitudes on the dayside (due to dayside compression of the geomagnetic field) and because there is a steep negative radial gradient in trapped MeV proton fluxes near geosynchronous. The higher flux level from the east-facing detector is due to the steep negative radial flux gradient in combination with a large gyroradius effect: The protons entering the east-facing detector have gyro centers inside of the geosynchronous orbit, while particles entering the west-facing detector have gyro-orbits mainly outside of geosynchronous. The difference between the east and west FOV fluxes can be used to estimate the radial gradient in magnetospheric and/or solar proton fluxes (Blake et al., 1974; Rodriguez et al., 2010; Walker et al., 1976).

6.3. SGPS Observations of CIR-Accelerated Ion Events

Beginning on January 30, 2017, SGPS observed the first in a series of corotating interaction region (CIR) proton events, recurring on the ~27-day solar rotation period during the declining phase of solar cycle 24 and continuing into the first half of 2018 with diminishing intensity. Ions are accelerated to energies up to ~20 MeV by CIR-associated shocks formed at the front boundary of high speed solar wind streams originating in coronal holes (Richardson, 2004; Gómez-Herrero et al., 2009, and references therein). The 2017–2018 SGPS CIR event observations are characterized by elevated flux levels up to P4 (6.5–12 MeV) energies, typically lasting several days to a week.

Figure 3 shows an example of a CIR proton event during April 21–27, 2017. One-hour Level 2 fluxes from the ACE Low Energy Magnetic Spectrometer (LEMS) P7 (1.06–1.91 MeV ions) and P8 (1.91–4.75 MeV ions) channels are shown in the top panel. Five-minute averaged fluxes from SGPS−X (west viewing) P1–P5 channels are shown in the middle panel. The enhancement in proton fluxes appears at energies up to 6.5–12 MeV. There is no discernable enhancement in the P5 channel (12–25 MeV). There is also no enhancement seen in the hourly OMNI >10 MeV 1AU proton flux shown in the bottom panel.

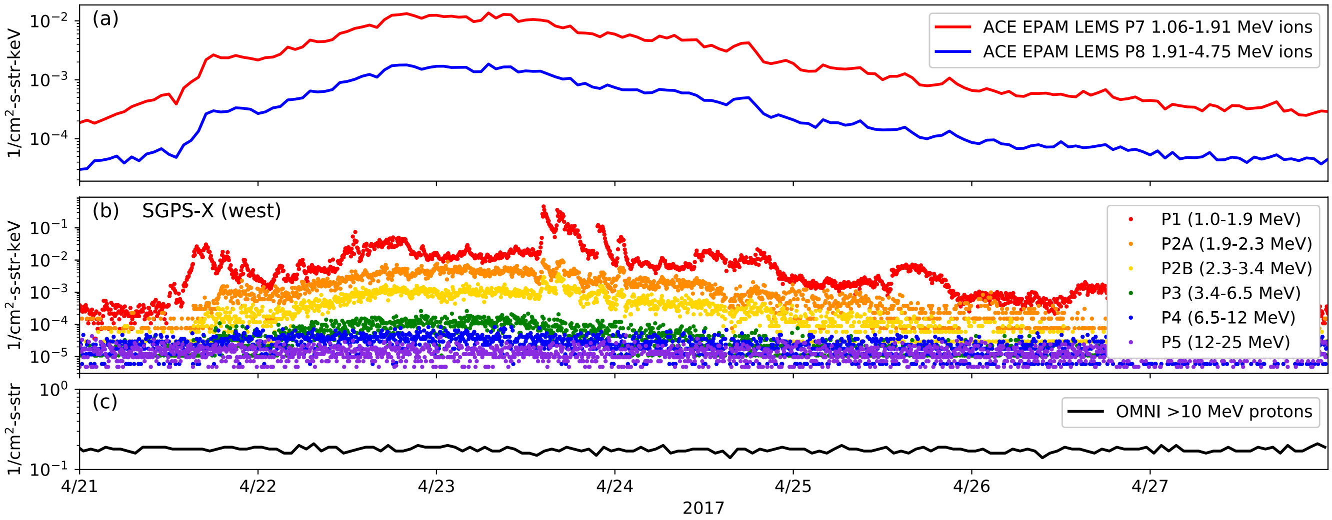

Figure 3. April 21–27, 2017 corotating interaction region (CIR) proton event observations, including 1-h level 2 fluxes from the ACE Low Energy Magnetic Spectrometer (LEMS) P7 (1.06–1.91 MeV) and P8 (1.91–4.75 MeV) ion channels (a), 5-min averaged fluxes from SGPS−X (west viewing) P1–P5 channels (b), and hourly OMNI >10 MeV 1AU proton flux (c). The CIR-associated proton enhancement appears at energies up to 6.5–12 MeV in the SGPS data, and there is no enhancement seen in the SGPS P5 (12–25 MeV) or OMNI >10 MeV proton fluxes (ACE data from R. Gold at JHU/APL and OMNI data from J. H. King, N. Papitashvili, ADNET, NASA GSFC; both via CDAWeb at https://cdaweb.gsfc.nasa.gov/index.html/).

7. September 2017 SEP Events Data Set

The first SPE following GOES-16 launch occurred in July 2017. A medium-sized (M2) solar flare and a coronal mass ejection (CME) erupted from the same active region of the sun on July 14th. An associated SPE arrived at Earth ~5 UT on July 14th, returning to near background levels on July 21st. The July 2017 SPE had a soft spectrum (relative to the September 2017 SPEs), with significant response only in the SGPS T1 energy channels. During September 2017, a series of M- and X-class solar flares produced several SPEs (Redmon et al., 2018). The first discernable response to SEPs in SGPS T3 was observed on September 6th. This was followed by a GLE on September 10th, the second GLE recorded in solar cycle 24 (The first was on May 17, 2012). At the time of writing, there have been no SPEs since September 2017.

The complete September 2017 GOES-16 SGPS data set of 5-min averaged fluxes is shown in Figure 4. SEP enhancements appear on the 4th, 6th, and 10th. Energetic storm particle (ESP) events, accompanying interplanetary shock arrivals at Earth, are seen near 0 UT on September 7th and 8th. The ESP particles are produced by local acceleration of ions by the interplanetary shock front (Bryant et al., 1962; Mäkelä et al., 2011).

An expanded view of the 10–13 September period is included in Figure 5 to highlight noteworthy features in the data set. There are several significant differences between the east and west FOV fluxes:

1. On September 10th, a more rapid onset of the SPE is seen in the west FOV than in the east FOV. This is typical, since solar protons entering the west-facing detector are less influenced by geomagnetic shielding. The best practice is to use fluxes from the westward-facing detector to drive, for example, PCA models (Rose & Ziauddin, 1962; Sauer & Wilkinson, 2008), since the flux from the westward-viewing detector at geosynchronous provides a more accurate proxy for the interplanetary and polar cap region flux.
2. Time-dependent structures immediately following SPE onset are seen in the west FOV on September 10th at energies up to 150–275 MeV (P9). The appearance of such structures in the west FOV but not in the east FOV at energies well above the cutoff suggests inhomogeneity or anisotropy in interplanetary space, such as an Interplanetary Magnetic Field (IMF)-aligned population arriving from the sunward direction along IMF lines.
3. Suppression of fluxes due to geomagnetic shielding appears up to 6.5–12.5 MeV (P4) in the west FOV and up to 40–80 MeV (P7) in the east FOV, near 18 UT when GOES-16 is at noon LT. The energy-LT dependence of the cutoffs is also seen; for example, in SGPS+X P2A-P7 on 9/12 ~18 UT, suppression of higher energies appears earlier than suppression of lower energies. This is because larger gyro radii ions traversing

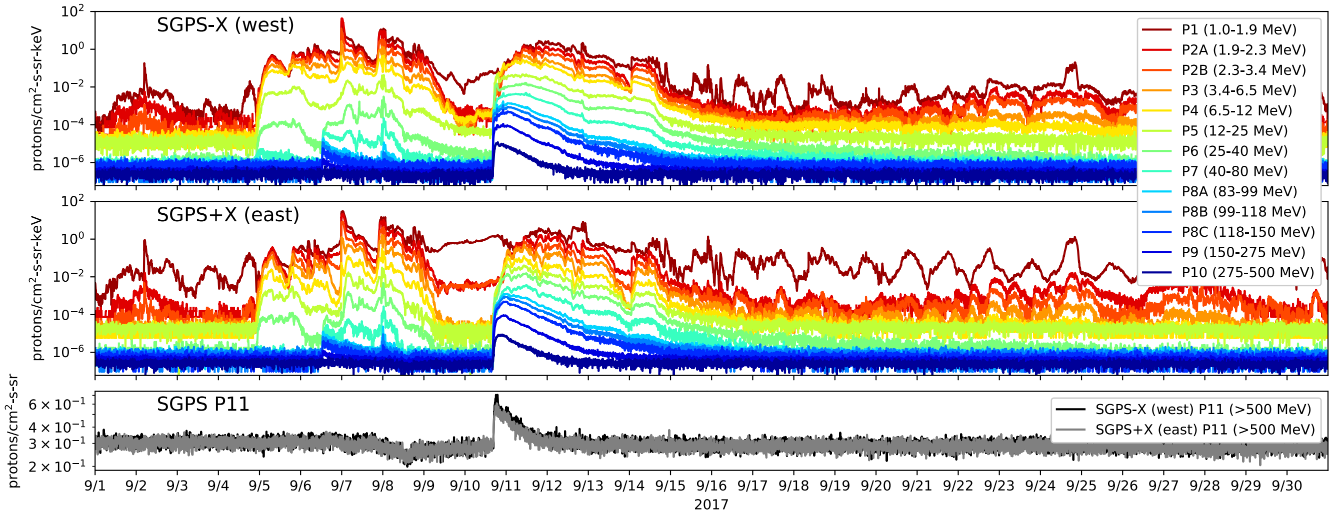

Figure 4. Full Solar and Galactic Proton Sensor (SGPS) September 2017 data set available from the National Oceanic and Atmospheric Administration-National Centers for Environmental Information Geostationary Operational Environmental Satellites-R website, including P1–P10 (differential) and P11 (>500 MeV) integral fluxes from east- and west-facing SGPS units.

the enhanced noon LT geomagnetic field during the radially inward bound portion of their orbit arrive at geosynchronous east of those with smaller gyro radii. There was no significant geomagnetic storm activity during this period ($Dst > -35$), and so these cutoffs are representative of quiet, nonstorm-time cutoffs.

A Forbush decrease (Forbush, 1937) preceding the GLE is seen in the P11 (> 500 MeV) fluxes shown in the bottom panel of Figure 4, following the interplanetary CME arrival at 1 AU on September 8th. The Forbush decrease is due to suppression of GCR entry into the heliosphere caused by interplanetary disturbances accompanying the CME.

The complete September 2017 SGPS data set is available from the NOAA-NCEI website at https://www.ngdc.noaa.gov/stp/satellite/goes-r.html under the special events tab. Corrections for temperature dependence in SGPS−X T1 P2A-P5 and T3 P8C-P11, anomalously low response in SGPS+X P7, and electron contamination

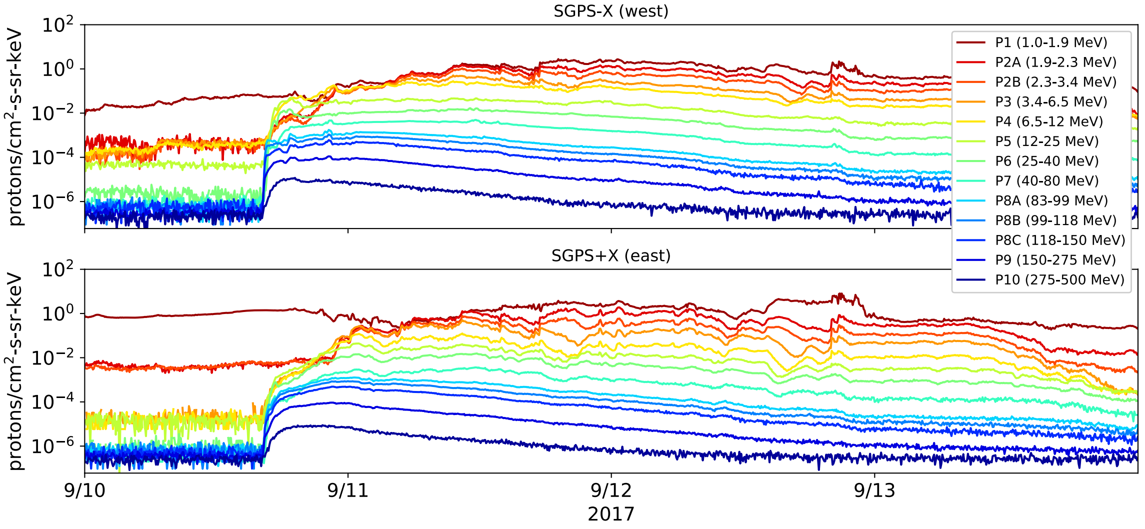

Figure 5. September 10–13, 2017 SEP event (GLE) fluxes from Geostationary Operational Environmental Satellites-16 Solar and Galactic Proton Sensor (SGPS) P1–P10 (all differential channels) from east- and west-facing SGPS units. Significant differences between fluxes from the east- and west-facing units include a more rapid onset and higher peak fluxes in general in the west field of view (FOV) and greater suppression of fluxes due to geomagnetic shielding, up to 40–80 MeV (P7), in the east FOV.

in SGPS+X P5 were performed on the September 2017 data set. The temperature dependence correction is described below in Appendix A.

8. Cross-Instrument Comparisons

Assuming a homogeneous and isotropic SEP distribution in interplanetary space, the SEP cross-instrument calibrations are valid for comparisons between channels with bandpass energies exceeding local proton cutoff energies at respective spacecraft locations and corresponding to look directions within the detector FOVs (Kress et al., 2013). The proton cutoff energy is the threshold energy below which the solar protons are geomagnetically shielded. Geomagnetic cutoff is a function of location, direction of arrival, and geomagnetic activity. At energies below the proton cutoff energy, there are natural, geophysical differences between measurements made at different LTs and/or in different look directions. Suppression of proton fluxes due to geomagnetic cutoffs are not exhibited above ~80 MeV (e.g., seen in Figure 5); so direct comparisons between SGPS−X and +X units and with GOES 13–15 EPS are valid at T3 channel energies but not necessarily at T1 and T2 energies.

At SPE onset, the most field-aligned and energetic SEPs are the first to arrive at 1 AU, resulting in an initially anisotropic distribution with a very hard spectrum. A hard spectrum increases contribution to reported fluxes from the high energy tail portion of the channel response functions, causing significant out-of-band contamination in some channels. During the peak and declining portion of the SPE, the spectrum becomes softer and the flux becomes isotropic (Reid, 1964; Desai & Giacalone, 2016).

Based on the considerations above, the period September 11–14, 2017 is used for the T3 cross-calibrations, beginning at 7:30 UT on September 11th near the peak flux in the P8 energy channels ~15 h after event onset and ending when the SGPS 5-min averages first drop below the background level. Cross-calibrations between SGPS units and with GOES-13 and -15 are performed for all T3 differential channels. The cross-satellite comparisons reveal significant systematic differences between SGPS and EPS measurements at T3 energies.

Figure 6 shows a comparison of GOES-16 SGPS, GOES-13 EPS, and GOES-15 EPS spectra at 7:30 UT on September 11, 2017. This time snapshot is near the peak proton flux in the 10–100 MeV range. Effective energies used in Figure 6 are determined using the method outlined in steps 1–4 in Section 5. The SGPS T3 (80–500 MeV) reported fluxes are about a factor of two higher than the EPS measurements. There is better agreement at SGPS T1 and T2 energies (1–80 MeV). Noteworthy exceptions are GOES-15 EPS P2 east, which is a factor of ~3 less than the other measurements, and P4 fluxes from the SGPS+X and −X units which differ by a factor of ~3.

8.1. SGPS Telescope-3 Cross-Calibrations

Cross-calibrations between SGPS and EPS measurements were performed to quantify systematic differences between their reported fluxes. Since the EPS P1–P7 energy channels do not align with SGPS energy channels, a power law is fit to the EPS fluxes, and SGPS fluxes are compared with the EPS spectrum at SGPS channel effective energies. The EPS power law fit and SGPS channel effective energies are obtained using the iterative method (steps 1–4) presented in Section 5. The EPS energy bounds from Sandberg et al. (2014), determined from cross-calibrations with NASA's IMP-8 Goddard Medium Energy Experiment (GME), are used to obtain the EPS effective energies. SGPS channel energy bounds E_L and E_U given in Appendix B are used to obtain the SGPS effective energies.

An example scatter plot showing the comparison between GOES-13 EPS and GOES-16 SGPS−X P8C is shown in Figure 7 using linear and log scales in the left and right panels, respectively (i.e., the same data are shown in both panels). The points included in the scatter plots are simultaneous 5-min averages between 7:30 UT September 11th and 0 UT September 17th, including samples up to when fluxes first drop below the background level. The spectral slope between EPS P6 and P7 is extrapolated for comparison with SGPS P9 and P10 effective energies.

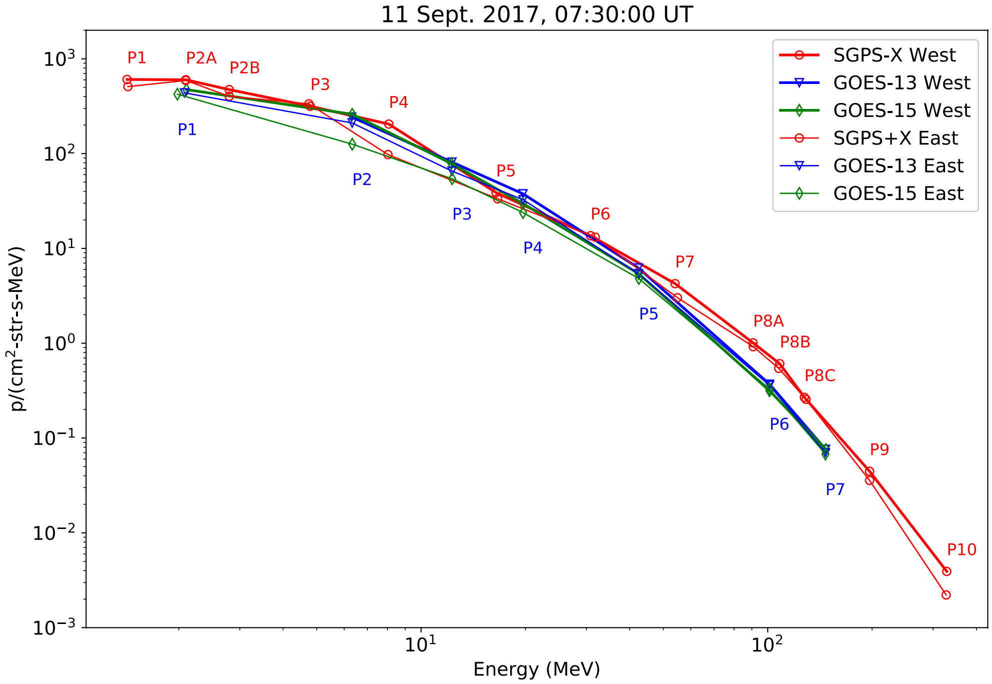

Figure 6. Comparison of spectra from Geostationary Operational Environmental Satellites (GOES)-16 Solar and Galactic Proton Sensor (SGPS), GOES-13 Energetic Particle Sensor (EPS), and GOES-15 EPS at 7:30 UT near the event peak flux during the September 2017 GLE. GOES-16, GOES-13, and GOES-15 measurements are shown with red, blue, and green traces, respectively. East and west fluxes are shown by the thin and thick traces, respectively. Effective energies are determined using the method outlined in steps 1–4 in Section 5. Note, west-facing GOES-13 P1 channel (P1B) measurements have not been available since March 2017 due to a noise issue affecting EPEAD's front detector (described in "GOES-13 P1B Failure March 2017.pdf" at https://www.ngdc.noaa.gov/stp/satellite/goes/dataaccess.html).

Uncorrected EPS and SGPS fluxes (without background removal) are used in the comparisons. This is done for two reasons: (1) an SGPS data set with background removal is not available and (2) the corrected EPS fluxes available from NOAA-NCEI have discontinuities near but above background levels due to inherent features in

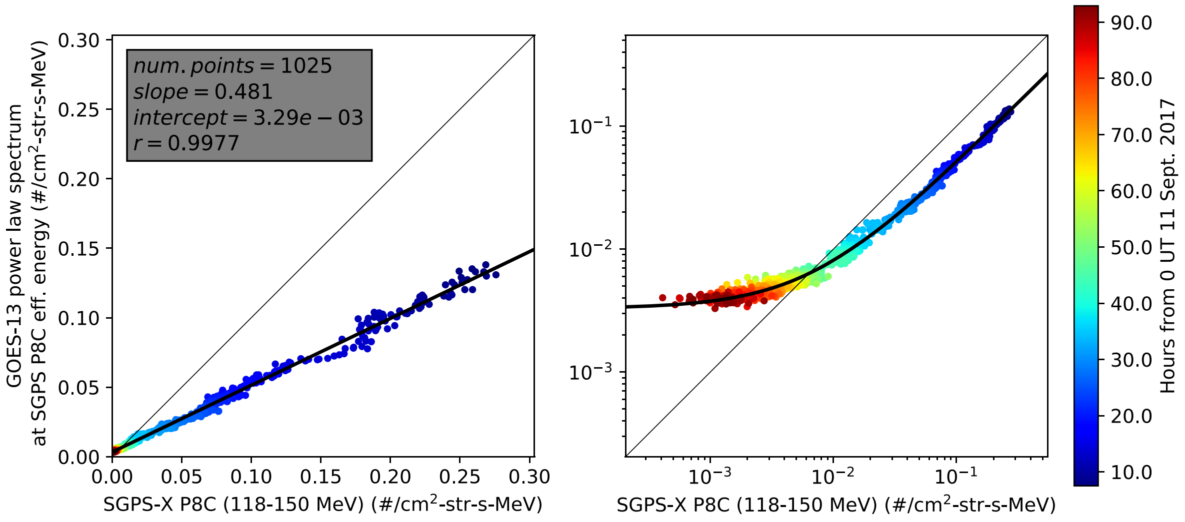

Figure 7. Geostationary Operational Environmental Satellites (GOES)-13 West versus Solar and Galactic Proton Sensor (SGPS)−X P8C scatter plots of simultaneous 5-min averages from 11 to 16 September 2017 using linear and log scales. A power law is fit to the EPS fluxes, and comparisons with the EPS spectrum are made at SGPS channel effective energies. The same data and OLS fit are shown in both panels.

Table 2
OLS Fit Parameters From EPS Versus SGPS Scatter Plots of Simultaneous 5-min Averaged Fluxes From 11 to 16 September 2017, Including the Following: Number of Samples, Slope, Intercept, and Correlation Coefficient

	GOES-13 EPS versus SGPS				GOES-15 EPS versus SGPS			
Channel	Num.	Slope	Intercept	*R*	Num.	Slope	Intercept	*R*
SGPS−X P8A	1,637	0.489	6.26e-03	0.9988	1,637	0.418	5.56e-03	0.9984
SGPS−X P8B	1,431	0.451	4.58e-03	0.9990	1,431	0.397	4.04e-03	0.9988
SGPS−X P8C	1,025	0.481	3.29e-03	0.9977	1,025	0.458	3.07e-03	0.9973
SGPS−X P9	962	0.442	1.15e-03	0.9961	963	0.519	1.28e-03	0.9961
SGPS−X P10	459	0.560	1.36e-04	0.9696	459	0.846	1.82e-04	0.9713
SGPS+X P8A	1,347	0.507	6.53e-03	0.9980	1,347	0.451	5.77e-03	0.9979
SGPS+X P8B	1,319	0.493	4.48e-03	0.9995	1,319	0.449	4.10e-03	0.9995
SGPS+X P8C	1,179	0.461	3.24e-03	0.9991	1,179	0.439	3.11e-03	0.9991
SGPS+X P9	876	0.481	1.07e-03	0.9961	877	0.509	1.14e-03	0.9962
SGPS+X P10	339	0.685	2.85e-05	0.9570	339	0.806	6.04e-05	0.9548

Note. Corresponding plots are included in the supplemental materials.

the background removal algorithm and in its implementation at the Space Weather Prediction Center [Rodriguez et al., 2017, Appendix A: Description of the Zwickl (1989) Algorithm].

The log scale plot is included to reveal the relation between the SGPS and EPS fluxes approaching background levels. The EPS background levels near 118–150 MeV are significantly higher than the SGPS−X P8C backgrounds. This holds true for EPS versus SGPS backgrounds in general in uncorrected fluxes at energies > 80 MeV.

An ordinary least squares (OLS) fit to the EPS versus SGPS fluxes is performed, yielding a mapping from SGPS flux to EPS flux

$$j_{\text{EPS}} = A_0\, j_{\text{SGPS}} + A_1 \tag{12}$$

The fit parameters A_0 and A_1 from all SGPS T3 cross-comparisons with EPS are given in Table 2. The complete set of scatter plots showing all SGPS-EPS cross-comparisons and linear fits are included in the supplemental materials at https://www.ngdc.noaa.gov/stp/space-weather/satellite-data/satellite-systems/goesr/solar_proton_events/sgps_sep2017_event_data/eps_sgps_comparison_plots/

Direct comparisons between the SGPS−X and +X units were also performed. The SGPS T3 cross-unit calibration results are given in Table 3. In general, the reported GOES-16 SGPS−X P8 fluxes are ~10% higher, P9 ~20% higher, and P10 ~40% higher than the SGPS+X fluxes. The corresponding scatter plots are included in the supplemental materials.

Table 3
OLS Fit Parameters From SGPS+X Versus SGPS−X Scatter Plots of Simultaneous 5-min Averaged T3 Fluxes From September 11 to 16, 2017, Including the Following: Number of Samples, Slope, Intercept, and Correlation Coefficient

Channel	Num.	Slope	Intercept	*R*
P8A	1,465	0.885	−5.96e-04	0.9970
P8B	1,131	0.880	1.54e-04	0.9981
P8C	1,128	0.914	−1.90e-04	0.9966
P9	889	0.819	1.11e-04	0.9963
P10	325	0.664	2.09e-04	0.9468

Note. Corresponding plots are included in the supplemental materials.

8.2. Cross-Calibrations at SGPS T1 and T2 Energies

The range of energies over which the SGPS-EPS comparisons are free from magnetospheric effects is limited by the lower energy bound of the two EPS energy channels bounding the SGPS effective energy. If this lower bound is below the geomagnetic cutoff at any point along the spacecraft orbit, then the flux is suppressed below the interplanetary flux. Magnetospheric effects are evident in comparisons between SGPS and EPS at SGPS T1 and T2 energies (~1–80 MeV); for example, the effect of heightened cutoffs near noon LT appears as fluctuations above or below the linear fit. The SGPS-EPS scatter plots and linear fits at SGPS T1 and T2 energies are not shown here but are included in the supplemental material. The T1 and T2 cross-comparisons show systematic differences between SGPS and EPS reported fluxes similar to differences seen in Figure 6.

Ideally, cross-comparisons at SGPS T1 and T2 energies would be performed during a period of strong geomagnetic activity when cutoffs are sufficiently suppressed and there is uniform isotropic flux at geosynchronous. Rodriguez et al. (2014) show that during periods when the solar wind dynamic pressure $P_{dyn} > 10$ nPa, the cutoff is suppressed sufficiently for cross-calibration of EPS channels ≥4.2–8.7 MeV. The September 2017 GLE did not include strong geomagnetic activity. The July 2017 SPE, however, included an ~ 1 hour period of $P_{dyn} > 10$ nT followed by continuing elevated P_{dyn} (5–10 nP) and $Dst < -50$. The soft spectrum during the July 2017 SPE limits these comparisons to SGPS P1–P4. The July and September 2017 cross comparison results at SGPS T1 and T2 energies should be used with caution.

9. Corrections and Caveats

A listing of L1b data caveats is given in the GOES-16 and -17 SGPS readme files on NCEI's website (https://data.ngdc.noaa.gov/platforms/solar-space-observing-satellites/goes/goes16/l1b/seis-l1b-sgps/ReadMe_SGPS-L1b_Provisional_Maturity.pdf). These cautions do not all apply to the September 2017 data set that has been corrected for SGPS−X temperature dependence, anomalously low response in SGPS+X P7, and electron contamination in SGPS+X P5.

Uncorrected SGPS+X P7 fluxes from the September 2017 SEP events are up to a factor of 6 low in comparisons with neighboring channels; for example, reported SGPS+X P7 fluxes are within a few percent of SGPS+X P8A fluxes during the declining phase of the September 2017 GLE. Analysis under different spectral conditions show that SGPS+X P7 has both a higher energy passband and a smaller geometric factor than was determined from beam calibrations. Estimates of the channel energy bounds and geometric factor were obtained using forward modeling of the P7 channel and minimization of differences with SGPS−X P7 and spectral fits to neighboring channels under different spectral conditions. A simplified version of the spectrally dependent temperature correction presented in Appendix A has been applied to SGPS+X P7 in the September 2017 data set, where the fixed, empirically determined values for P7 E_L, E_U, and G_0 are used in the denominator of A2, and A3 is used to correct the P7 count rate.

When there is no SPE in progress and the outer electron radiation belts are enhanced, electron contamination is seen in SGPS+X P5 near the background level (not shown in this paper). When the radiation belt fluxes are particularly enhanced (e.g., SWPC GOES > 2 MeV electrons ~ 10^4-10^5 e^-/cm^2-s-sr), an enhancement of up to a factor of ~2–3 above background levels is seen, with diurnal variations characteristic of GOES radiation belt observations. The source of contamination is believed to be a chance double coincidence triggered by two electrons in two adjacent T1 detectors. It is not known why the +X unit is susceptible to this contamination and the −X unit is not. An effective correction for the electron contamination using SGPS T1 singles rates was developed at ATC. Since the effect of the electron contamination produces a < 1% contribution to the total P5 flux during a small-to-moderate SPE, the correction is not implemented in L1b processing. This correction *has* been applied to the September 2017 data set.

In addition to systematic differences with GOES EPS measurements presented in Section 8, the following caveats apply to the September 2017 data set:

1. As noted in Section 6 above, SGPS background levels in channels P3–P9 are significantly higher than GCR fluxes. During non-SPE periods, channels P3–P9 do not accurately report GCR fluxes.
2. SGPS−X and +X P4 reported fluxes differ by about a factor of 3 during a period of high solar wind dynamic pressure during the July 2017 SPE when we expect east and west SEP fluxes at geosynchronous to be similar. A factor of ~ 3 difference is also seen in Figure 6 during the September 2017 GLE. It is not known which P4 channel is more accurate.
3. The P5 high energy island ~ 100 MeV seen in the top panel of Figure 1 is a significant source of out-of-band contamination that is not currently corrected for. A correction has been implemented in L1b processing to remove the P5 out-of-band counts using P7 and P8A measurements, but it is not currently used. Work is ongoing to fully characterize the P5, P7, and P8 response functions for development of the P5 correction (Note, P5 backgrounds seen in Figure 4 are higher than neighboring channels mainly due to GCR counts picked up by the P5 high energy island.)

10. Summary and Discussion

SGPS monitors hazards to spacecraft systems and humans in space from 10 to 100s of MeV protons during SPEs serving in the same capacity as the first EPS flown on board NOAA's geosynchronous weather satellites SMS-1 and -2 (1974–1976). The same EPS/EPEAD design has been flown on GOES-4 through -15 (excepting a detector redesign on GOES-8), providing measurements of 0.74–900 MeV protons in 7 logarithmically spaced energy channels. SGPS has higher energy resolution and greater dynamic range than EPS, with 13 channels spanning 1–500 MeV and background levels up to an order of magnitude lower than EPS. The cross-calibrations between SGPS and EPS measurements presented here and in the supplemental material are needed for determining systematic differences in calibration and to aid in establishing a continuous self-consistent data set of GOES SPE measurements.

The SGPS differential channels were designed and calibrated to measure energy spectra with $\gamma \gtrsim 1.8$ (in Equation 8). The differential channels have nonzero response well above their nominal upper energy bounds that makes them susceptible to out-of-band contamination from higher energy protons. Channels P1–P9 do not provide accurate measurements under conditions where the spectral slope is flat or rising with energy, for example, a GCR spectrum or during SPE onset. The P11 >500 MeV integral channel mainly measures GCRs, which can be a source of SEEs in electronics and are of concern for missions involving humans in space for long periods.

The east- and west-facing SGPS units provide a full view of SEP cutoffs at geosynchronous in quiet geomagnetic fields during the September 2017 GLE. At energies above ~2 MeV, there is little to no geomagnetic shielding of solar protons except near noon LT. Near noon LT, proton cutoff energies at geosynchronous are ~6.5–12.5 MeV for protons arriving from the east and ~40–80 MeV for protons arriving from the west.

The cross-calibrations reveal significant systematic differences between SGPS and EPS measurements. In general, SGPS reports higher fluxes than EPS at a given energy. SGPS T3 (83–500 MeV) fluxes exceed the EPS measurements by approximately a factor of two. The cross-comparisons between SGPS and EPS at energies below ~80 MeV are less reliable due to (1) small numbers of samples with fluxes sufficiently elevated above backgrounds during the July 2017 SEP event and (2) LT-dependent suppression of fluxes due to geomagnetic effects in one or both of the units under comparison during the September 2017 SEP events. Some general results from the comparisons at SGPS T1 and T2 energies (1–80 MeV) are

1. SGPS P7 is 1.4–2x higher than EPS.
2. SGPS P6 is 1.1–1.6x higher than EPS.
3. G13 EPS is 1.2–1.3x higher than SGPS P5. G15 EPS is generally in agreement with SGPS P5.
4. SGPS−X P4 is a factor of 2.5–4.5 higher than SGPS+X P4. The EPS measurements span the range between the SGPS−X and +X reported fluxes.
5. SGPS has significantly lower backgrounds, with the transition from higher SGPS SEP event fluxes to higher EPS fluxes as EPS approaches background level.

For more specific results, see the supplemental data at https://www.ngdc.noaa.gov/stp/space-weather/satellite-data/satellite-systems/goesr/solar_proton_events/sgps_sep2017_event_data/eps_sgps_comparison_plots/

In addition to supporting real-time alerts at SWPC, SGPS data will provide valuable data sets to the space science community, advancing basic space science research, first-principles space weather modeling and forecast, and understanding of space weather effects on spacecraft systems and humans in space. As with its predecessor EPS, post-operational data from SGPS will be made publicly available at NOAA-NCEI and other data services. The September 2017 data set currently available at NCEI's website has been corrected for SGPS−X temperature dependence and anomalously low response in SGPS+X P7. In 2021, these corrections will be implemented in NCEI's GOES-R Level-2 processing, providing Solar Cycle 25 SPE data in near real time.

Appendix A: SGPS Temperature Dependence Correction

Corrections for temperature dependence in SGPS−X T1 P2A-P5 and T3 P8C-P11 were performed on the September 2017 data set. The temperature correction is based on a rectangular function model of the energy channel response function (5) and a power law model of the ambient spectrum (8). Using these models, the total counts/sec. in the channel from the convolution (9) is

$$C = G_0 j_0 \frac{E_U^{1-\gamma} - E_L^{1-\gamma}}{(1-\gamma)} \tag{A1}$$

The ratio of the counts in the fixed/calibrated channel (at $T = 25°C$) to counts in the temperature-dependent channel,

$$X = \frac{G_0(T = 25°C)\left[E_U(T = 25°C)^{1-\gamma} - E_L(T = 25°C)^{1-\gamma}\right]}{G_0(T)\left[E_U(T)^{1-\gamma} - E_L(T)^{1-\gamma}\right]}, \tag{A2}$$

is used to correct the temperature-dependent count rates, that is,

$$C_{\text{reported}} = XC(T). \tag{A3}$$

The fixed energy boundaries G_0, E_U, and E_L at $T = 25°C$ are obtained from ground calibrations, and the temperature-dependent energy boundaries $G_0(T)$, $E_U(T)$, and $E_L(T)$ are obtained empirically, by demanding removal of temperature-dependent fluctuations under different spectral conditions.

The temperature correction algorithm first iteratively fits a single power law to 5-min averaged fluxes from nontemperature-dependent channels nearby the channel being corrected to obtain γ, then channel energy boundaries are interpolated using instrument temperatures obtained from Level-0 data, and these are used in A2.

Appendix B: GOES-16 and -17 SGPS Geometric Factors and Energy Band Boundaries

The geometric factors (G_0), geometric factor error (σ_G) and energy band boundaries (E_L and E_U) used in SGPS GOES-16 and -17 SGPS ground processing are given in Tables B1 and B2. These parameters are obtained from GEANT simulation results scaled to minimize RMS differences with ground/beam calibrations as described in

Table B1
GOES-16 SGPS Geometric Factors and Energy Band Boundaries

	GOES-16 SGPS−X				GOES-16 SGPS+X			
Channel	G_0 (cm^2-sr)	σ_G (cm^2-sr)	E_L (MeV)	E_U (MeV)	G_0 (cm^2-sr)	σ_G (cm^2-sr)	E_L (MeV)	E_U (MeV)
P1	0.11	0.024	1.02	1.86	0.11	0.024	1.02	1.86
P2A	0.11	0.024	1.90	2.30	0.11	0.024	1.90	2.30
P2B	0.11	0.024	2.31	3.34	0.11	0.024	2.31	3.34
P3	0.10	0.022	3.40	6.48	0.10	0.022	3.40	6.48
P4	0.11	0.024	5.84	11.0	0.11	0.024	5.84	11.0
P5	0.12	0.026	11.6	23.3	0.12	0.026	11.6	23.3
P6	0.48	0.078	24.9	38.1	0.43	0.075	25.9	39.1
P7	0.48	0.078	40.3	73.4	0.48	0.078	41.2	74.3
P8A	1.90	0.287	83.7	98.5	1.58	0.231	82.9	99.8
P8B	1.87	0.282	99.9	118	1.37	0.200	96.4	121.
P8C	1.15	0.173	115	143	1.03	0.150	114	148
P9	2.43	0.355	160	242	2.13	0.322	160	242
P10	1.27	0.192	276	404	1.27	0.192	276	404
P11	2.50	0.268	500		2.50	0.268	500	

GOES, Geostationary Operational Environmental Satellites; SGPS, Solar and Galactic Proton Sensor.

Table B2
GOES-17 SGPS Geometric Factors and Energy Band Boundaries

	GOES-16 SGPS−X				GOES-16 SGPS+X			
Channel	G_0 (cm^2-sr)	σ_G (cm^2-sr)	E_L (MeV)	E_U (MeV)	G_0 (cm^2-sr)	σ_G (cm^2-sr)	E_L (MeV)	E_U (MeV)
P1	0.11	0.024	1.02	1.86	0.11	0.024	1.02	1.86
P2A	0.11	0.024	1.90	2.30	0.11	0.024	1.90	2.30
P2B	0.11	0.024	2.31	3.34	0.11	0.024	2.31	3.34
P3	0.10	0.022	3.40	6.48	0.10	0.022	3.40	6.48
P4	0.11	0.024	5.84	11.0	0.11	0.024	5.84	11.0
P5	0.12	0.026	11.6	23.3	0.12	0.026	11.6	23.3
P6	0.41	0.054	23.9	32.6	0.51	0.067	25.8	34.2
P7	0.44	0.070	40.7	68.2	0.42	0.066	41.0	74.1
P8A	1.37	0.200	83.9	98.4	1.35	0.194	83.9	98.4
P8B	1.40	0.200	99.7	118	1.37	0.197	99.7	118
P8C	0.72	0.100	123	148	1.01	0.145	117	144
P9	1.39	0.220	156	237	1.28	0.205	156	237
P10	1.31	0.210	267	390	1.31	0.206	267	390
P11	2.50	0.270	500		2.50	0.270	500	

Section 3. Not all SGPS channels in GOES-16 and -17 SGPS+X and −X units are ground calibrated in a particle beam, and in some cases, values obtained from one unit are used for all units (e.g., P1–P5). Reported fluxes are obtained using $j = C / (G_0 \Delta E)$, where $\Delta E = E_U - E_L$. The values given here are subject to change if sufficient evidence from cross-calibrations with similar measurements from other instruments warrants it but have not been changed since the launch.

Data Availability Statement

The September 2017 SGPS data set and additional supplemental materials are available at NCEI's website https://www.ngdc.noaa.gov/stp/satellite/goes-r.html under the special event data tab.

Acknowledgments
This work was supported by the GOES-R program and the National Centers for Environmental Information (NCEI) through NOAA Cooperative Agreements NA15OAR4320137 and NA17OAR4320101. Support was also provided by the Air Force Office of Sponsored Research (AFOSR) under grant FA9550-20-1-0339.

References

Agostinelli, S., Allison, J., Amako, K., Apostolakis, J., Araujo, H., Arce, P., et al. (2003). GEANT4–a simulation toolkit. *Nuclear Instruments and Methods*, *506*(3), 256–303. https://doi.org/10.1016/S0168-9002(03)01368-8

Blake, J. B., Martina, E. F., & Paulikas, G. A. (1974). On the access of solar protons to the synchronous altitude region. *Journal of Geophysical Research*, *79*(10), 1345–1348. https://doi.org/10.1029/JA079i010p01345

Bryant, D. A., Cline, T. L., Desai, U. D., & McDonald, F. B. (1962). Explorer 12 observations of solar cosmic rays and energetic storm particles after the solar flare of September 28, 1961. *Journal of Geophysical Research*, *67*, 4983–5000. https://doi.org/10.1029/JZ067i013p04983

Clilverd, M. A., Rodger, C. J., Ulich, T., Seppälä, A., Turunen, E., Botman, A., & Thomson, N. R. (2005). Modeling a large solar proton event in the southern polar atmosphere. *Journal of Geophysical Research: Space Physics*, *110*, A09307. https://doi.org/10.1029/2004JA010922

Desai, M., & Giacalone, J. (2016). Large gradual solar energetic particle events. *Living Reviews in Solar Physics*, *13*, 3. https://doi.org/10.1007/s41116-016-0002-5

Dichter, B. K., Galica, G. E., McGarity, J. O., Tsui, S., Golightly, M. J., Lopate, C., & Connell, J. J. (2015). Specification design and calibration of the space weather suite of instruments on the NOAA GOES-R program spacecraft. *IEEE Transactions on Nuclear Science*, *62*(6), 2776–2783. https://doi.org/10.1109/TNS.2015.2477997

Dyer, C. S., Lei, F., Clucas, S. N., Smart, D. F., & Shea, M. A. (2003). Calculations and observations of solar particle enhancements to the radiation environment at aircraft altitudes. *Advances in Space Research*, *32*(1), 81–93. https://doi.org/10.1016/s0273-1177(03)90374-7

Forbush, S. E. (1937). On the effects in cosmic-ray intensity observed during the recent magnetic storm. *Physical Review*, *51*, 1108–1109. https://doi.org/10.1103/physrev.51.1108.3

Gómez-Herrero, R., Klassen, A., Müller-Mellin, R., Heber, B., Wimmer-Schweingruber, R., & Böttcher, S. (2009). Recurrent CIR-accelerated ions observed by STEREO SEPT. *Journal of Geophysical Research*, *114*, A05101. https://doi.org/10.1029/2008JA013755

Grubb, R. N. (1975). *The SMS/GOES space environment monitor subsystem. NOAA technical Memorandum ERL SEL-42*. Boulder, CO: Space Environment Laboratory.

Hanser, F. A. (2011). *EPS/HEPAD calibration and data handbook. Tech. Rep. GOESN-ENG-048D*. Carlisle, MA: Assurance Technology Corporation. Retrieved from http://www.ngdc.noaa.gov/stp/satellite/goes/documentation.html

Kress, B. T., Rodriguez, J. V., Mazur, J. E., & Engel, M. (2013). Modeling solar proton access to geostationary spacecraft with geomagnetic cutoffs. *Journal of Advance Space Research*, *52*, 1939–1948. https://doi.org/10.1016/j.asr.2013.08.019

Kress, B. T., Rodriguez, J. V., & Onsager, T. G. (2020). The GOES-R space environment in situ suite (SEISS): Measurement of energetic particles in geospace. In J. G. Steven, T. J. Schmit, J. Daniels, & R. J. Redmon (Eds.), *The GOES-R Series* (pp. 243–250). Elsevier. https://doi.org/10.1016/B978-0-12-814327-8.00020-2

Kronberg, E. A., & Daly, P. W. (2013). Spectral analysis for wide energy channels. *Geoscientific Instrumentation, Methods and Data Systems*, *2*, 257–261. https://doi.org/10.5194/gi-2-257-2013

Lario, D., Sanahuja, B., & Heras, A. M. (1998). Energetic particle events: Efficiency of interplanetary shocks as 50 keV E 100 MeV proton accelerators. *The Astrophysical Journal*, *509*, 415–434. https://doi.org/10.1086/306461

Mäkelä, P., Gopalswamy, N., Akiyama, S., Xie, H., & Yashiro, S. (2011). Energetic storm particle events in coronal mass ejection–driven shocks. *Journal of Geophysical Research*, *116*, A08101. https://doi.org/10.1029/2011JA016683

Matthiä, D., Berger, T., Mrigakshi, A. I., & Reitz, G. (2013). A ready-to-use galactic cosmic ray model. *Advances in Space Research*, *51*, 329–338. https://doi.org/10.1016/j.asr.2012.09.022

Mertens, C. J., Kress, B. T., Wiltberger, M., Blattnig, S. R., Slaba, T. S., Solomon, S. C., & Engel, M. (2010). Geomagnetic influence on aircraft radiation exposure during a solar energetic particle event in October 2003. *Space Weather*, *8*, S03006. https://doi.org/10.1029/2009SW000487

O'Neill, P. M., Golge, S., & Slaba, T. C. (2015). *Badhwar-O'Neill 2014 galactic cosmic ray flux model description*. NASA Technical Publication.

Raukunen, O., Paassilta, M., Vainio, R., Rodriguez, J. V., Eronen, T., Crosby, N., et al. (2020). Very high energy proton peak flux model. *Journal of Space Weather and Space Climate*, *10*, 24. https://doi.org/10.1051/swsc/2020024

Redmon, R. J., Seaton, D. B., Steenburgh, R., He, J., & Rodriguez, J. V. (2018). September 2017's geoeffective space weather and impacts to Caribbean radio communications during hurricane response. *Space Weather*, *16*(9), 1190–1201. https://doi.org/10.1029/2018sw001897

Reid, G. C. (1964). A diffusive model for the initial phase of a solar proton event. *Journal of Geophysical Research*, *69*(13), 2659–2667. https://doi.org/10.1029/JZ069i013p02659

Richardson, I. G. (2004). Energetic particles and corotating interaction regions in the solar wind. *Space Science Reviews*, *111*(3–4), 267–376. https://doi.org/10.1023/b:spac.0000032689.52830.3e

Rodriguez, J. V., Krosschell, J. C., & Green, J. C. (2014). Intercalibration of GOES 8-15 solar proton detectors. *Space Weather*, *12*, 92–109. https://doi.org/10.1002/2013SW000996

Rodriguez, J. V., Onsager, T. G., & Mazur, J. E. (2010). The east–west effect in solar proton flux measurements in geostationary orbit: A new GOES capability. *Geophysical Research Letters*, *37*, L07109. https://doi.org/10.1029/2010GL042531

Rodriguez, J. V., Sandberg, I., Mewaldt, R. A., Daglis, I. A., & Jiggens, P. (2017). Validation of the effect of cross-calibrated GOES solar proton effective energies on derived integral fluxes by comparison with STEREO observations. *Space Weather*, *15*, 290–309. https://doi.org/10.1002/2016SW001533

Rose, D. C., & Ziauddin, S. (1962). The polar cap absorption effect. *Space Science Reviews*, *1*(1), 115–134. https://doi.org/10.1007/bf00174638

Sandberg, I., Jiggens, P., Heynderickx, D., & Daglis, I. A. (2014). Cross calibration of NOAA GOES solar proton detectors using corrected NASA IMP-8/GME data. *Geophysical Research Letters*, *41*, 4435–4441. https://doi.org/10.1002/2014GL060469

Sauer, H. H., & Wilkinson, D. C. (2008). Global mapping of ionospheric HF/VHF radio wave absorption due to solar energetic protons. *Space Weather*, *6*, S12002. https://doi.org/10.1029/2008sw000399

Tylka, A. J., Cohen, C. M. S., Dietrich, W. F., Lee, M. A., Maclennan, C. G., Mewaldt, R. A., et al. (2005). Shock geometry, seed populations, and the origin of variable elemental composition at high energies in large gradual solar particle events. *The Astrophysical Journal*, *625*, 474–495. https://doi.org/10.1086/429384

Walker, R. J., Erickson, K. N., Swanson, R. L., & Winckler, J. R. (1976). Substorm associated particle boundary motion at synchronous orbit. *Journal of Geophysical Research*, *81*, 5541–5550. https://doi.org/10.1029/JA081i031p05541